Article:
(2024) Evaluation of the E2/M1 ratio in the N→ Δ(1232) transition from the γ- p- →pπ0 reaction. Physical Review C. 055201. ISSN 2469-9993

https://doi.org/10.1103/PhysRevC.109.055201

Editors' Suggestion

Evaluation of the $E2/M1$ ratio in the $N \rightarrow \Delta(1232)$ transition from the $\vec{\gamma}\vec{p} \rightarrow p\pi^0$ reaction

E. Mornacchi,[1] P. Pedroni,[2] F. Afzal,[3] Y. Wunderlich,[3] S. Abt,[4] P. Achenbach,[1] J. R. M. Annand,[5] H. J. Arends,[1] M. Bashkanov,[6] M. Biroth,[1] R. Beck,[3] N. Borisov,[7] A. Braghieri,[2] W. J. Briscoe,[8] F. Cividini,[1] C. Collicott,[1] A. Denig,[1] A. S. Dolzhikov,[7] E. Downie,[8] S. Fegan,[6] A. Fix,[9] D. Ghosal,[4] I. Gorodnov,[7] W. Gradl,[1] G. G. Gurevich,[10] L. Heijkenskjöld,[1] D. Hornidge,[11] G. M. Huber,[12] V. L. Kashevarov,[1] S. J. D. Kay,[6] M. Korolija,[13] A. Lazarev,[7] K. Livingston,[5] S. Lutterer,[4] I. J. D. MacGregor,[5] D. M. Manley,[14] P. P. Martel,[1] R. Miskimen,[15] M. Mocanu,[6] C. Mullen,[5] A. Neganov,[7] A. Neiser,[1] M. Oberle,[4] M. Ostrick,[1] P. B. Otte,[1] D. Paudyal,[12] A. Powell,[5] T. Rostomyan,[4] V. Sokhoyan,[1] K. Spieker,[3] O. Steffen,[1] I. I. Strakovsky,[8] M. Thiel,[1] A. Thomas,[1] Yu. A. Usov,[7] S. Wagner,[1] D. P. Watts,[6] D. Werthmüller,[6] J. Wettig,[1] L. Witthauer,[4] M. Wolfes,[1] and N. Zachariou[6]

(A2 Collaboration at MAMI)

[1]*Institut für Kernphysik, University of Mainz, D-55099 Mainz, Germany*

[2]*INFN Sezione di Pavia, I-27100 Pavia, Italy*

[3]*Helmholtz-Institut für Strahlen- und Kernphysik, Universität Bonn, D-53115 Bonn, Germany*

[4]*Department für Physik, Universität Basel, CH-4056 Basel, Switzerland*

[5]*SUPA School of Physics, Astronomy, University of Glasgow, Glasgow G12 8QQ, United Kingdom*

[6]*Department of Physics, University of York, Heslington, York Y010 5DD, United Kingdom*

[7]*Joint Institute for Nuclear Research, 141980 Dubna, Russia*

[8]*The George Washington University, Washington, District of Columbia 20052-0001, USA*

[9]*Tomsk Polytechnic University, 634034 Tomsk, Russia*

[10]*Institute for Nuclear Research, 125047 Moscow, Russia*

[11]*Mount Allison University, Sackville, New Brunswick, Canada E4L 1E6*

[12]*University of Regina, Regina, Saskatchewan, Canada S4S 0A2*

[13]*Rudjer Boskovic Institute, HR-10000 Zagreb, Croatia*

[14]*Kent State University, Kent, Ohio 44242-0001, USA*

[15]*University of Massachusetts, Amherst, Massachusetts 01003, USA*

(Received 27 November 2023; accepted 7 February 2024; published 6 May 2024)

A new data set for the helicity-dependent differential cross section of the single-meson photoproduction reaction $\gamma p \rightarrow p\pi^0$ was obtained for the photon energy interval 150–400 MeV. The experiment was performed at the A2 tagged photon facility of the Mainz Microtron MAMI using a circularly polarized photon beam and a longitudinally polarized proton target. The reaction products were detected with the large-acceptance Crystal Ball and TAPS calorimeters covering 97% of the full solid angle. These new results, obtained with a fine energy and polar angle binning, greatly increase both the existing quantity and quality of the data available for this observable. A moment analysis, based on a finite expansion in Legendre polynomials, was applied to these data by using a bootstrap-based fitting method to correctly account for their systematic uncertainties. From the resulting decomposition of the differential cross sections, the $E2/M1$ ratio for the $N \rightarrow \Delta(1232)$ transition was determined to be $[-2.38 \pm 0.16(\text{stat.}+\text{sys.}) \pm 0.10\ (\text{model})]\%$. Combining this value with previous results also allowed us to evaluate the most precise available estimate of the $E2/M1$ ratio to be used for all further reference and model comparisons.

DOI: 10.1103/PhysRevC.109.055201

I. INTRODUCTION

Fundamental states of hadrons are characterized by complex quark-gluon and meson cloud dynamics, which are governed by nonperturbative QCD and give rise to nonspherical components in their hadronic wave function. Precise experimental determination of the shapes then gives deep insight into these interactions and provides a fundamental precision benchmark for all types of models describing the hadronic structure (see, for instance, Refs. [1,2] and references therein).

The most direct and reliable evidence of a shape deformation is provided by the determination of the particles' electric quadrupole moments. However, the proton, the only stable hadron, has a vanishing spectroscopic quadrupole moment in the laboratory frame due to its spin-1/2 nature. Therefore, one has to study the transition to its lowest $J = 3/2$ excited state, namely, the $\Delta(1232)$ resonance.

The $N \rightarrow \Delta(1232)$ electromagnetic transition is predominantly due to the magnetic dipole component $M1$. In a very simple constituent quark model framework, this process is described by a spin flip of a single quark in the s-wave

state (see, for instance, Ref. [3] and references therein). Using real photons, any d-wave mixture in the nucleon and/or in the $\Delta(1232)$ wave functions allows for the electric quadrupole transition $E2$. Therefore, by measuring the $\gamma p \to \Delta(1232) \to N\pi$ reactions, one can assess the presence of the d-wave components and thus quantify to what extent the nucleon and/or the $\Delta(1232)$ resonance deviate from the spherical shape.

The amplitudes in the $\gamma N \to N\pi$ final states are usually described by the notations $E^I_{\ell\pm}$ and $M^I_{\ell\pm}$, where E and M are the electric and magnetic multipoles, respectively, ℓ is the orbital angular momentum of the photoproduced pion, the sign $\pm$ refers to the total $N\pi$ angular momentum $J = \ell \pm 1/2$, and I is the isospin of the $N\pi$ system.

A common practice (see again Ref. [3]) is to measure the resonant quadrupole strength relative to the resonant dipole amplitude via the ratio

$$R_{EM} = \frac{E2}{M1} \equiv \left.\frac{\mathrm{Im}\left[E^{3/2}_{1+}\right]}{\mathrm{Im}\left[M^{3/2}_{1+}\right]}\right|_{M_\Delta} \tag{1}$$

evaluated at the $\Delta(1232)$ mass value M_Δ.

Early empirical quark and Skyrme models, as well as relativistic models including two-body exchange currents, have given a variety of R_{EM} values in the range $-6\% < R_{EM} < 0\%$, where the minus sign indicates an oblate shape deformation (see, e.g., Refs. [4–6] and references therein).

More recently, a similar range of values was predicted by effective field theory approaches [7,8], dynamical and effective Lagrangian models [6,9–11], and the most recent lattice calculations [12].

From an experimental point of view, isolating the resonant E_{1+} amplitude is complicated by its rather small value compared to the dominant M_{1+} multipole transition. To overcome these difficulties, high-intensity photon beams of precisely known energy are required, along with the measurement of selected polarization observables that highlight the role of the small E_{1+} multipole thanks to the presence of interference terms between E_{1+} and the dominant M_{1+} multipole.

These conditions were met by the advent of a newer generation of tagged photon facilities in the late 1990s. In the past 20 years, several precision measurements have been performed at the photon tagging facility of the MAMI Microtron in Mainz (Germany) [13–16] and at the laser back-scattering facility (LEGS) of the Brookhaven National Laboratory (USA) [5], where R_{EM} was evaluated from both pion production and Compton scattering data.

The experimental apparatus of the LEGS Collaboration [5] had a complex geometry with a small angular acceptance and was best suited for photon detection. Measurements at the MAMI tagging photon facility have instead been performed over the years with different different detector setups: the large acceptance DAPHNE detector [13,14], covering the polar angle range $\theta_{\mathrm{lab}} \in [21^\circ, 159^\circ]$ with full azimuthal acceptance and good charged particle detection capabilites, and the TAPS (two-arm photon spectrometer) calorimeter [14] and the LARA apparatus [16], both suited for the photon detection, which had a complex geometry and somewhat limited geometrical acceptance, although they covered more extreme forward and backward angles compared to the LEGS apparatus.

All of these experiments have given estimates of R_{EM} that are compatible, within their errors, with the interval given by the latest Particle Data Group (PDG) estimate [17] of $-3\% \leqslant R_{EM} \leqslant -2\%$. A very similar interval ($R_{EM} = -2.5\% \pm 0.4\%$) has also been obtained from an analysis of the more recent $\gamma N \to N\pi$ data using the AMIAS methodology [18], a general-purpose algorithm applied for the analysis of several different hadronic and nuclear physics data sets [19,20].

In this paper, we present a new precise determination of the R_{EM} ratio from the measurement of the helicity-dependent differential cross section of the $\gamma p \to p\pi^0$ reaction in the incident photon energy range from 150 to 400 MeV. This experiment was performed at the A2 tagged photon facility of the MAMI electron accelerator in Mainz, Germany [21], using the experimental setup of the A2 Collaboration that combines all the strengths of the previous experiments described above: a very large ($\approx$97% of 4π) angular acceptance with a good energy and angular resolution for photons and protons, as well as a high photon detection efficiency. The measured double-polarization observable, accessed using a circularly polarized photon beam and a longitudinally polarized proton target, can be defined as

$$\frac{d\Delta\sigma}{d\Omega} = \left(\frac{d\sigma}{d\Omega}\right)_{3/2} - \left(\frac{d\sigma}{d\Omega}\right)_{1/2}, \tag{2}$$

where the subscripts $3/2$ and $1/2$ indicate the total helicity states of the γp system corresponding to the relative parallel or antiparallel photon-proton spin configurations, respectively.

Thanks to the very high statistics collected, it was possible to measure $d\Delta\sigma/d\Omega$ in very fine beam photon energy and polar angle binning, with a width of $\approx$2 MeV and 10°, respectively. This precise mapping of the entire $\Delta(1232)$ resonance excitation region greatly enhanced both the existing quantity and quality of the data available for this observable and allowed the existing estimates of the $E2/M1$ ratio to be improved using a Legendre-moment analysis.

The paper is organized as follows. In Secs. II and III, the experimental setup and the offline analysis methods used to obtain the measured observable are briefly described. In Sec. IV, the new results for $d\Delta\sigma/d\Omega$ are presented and compared with the scarce existing database. Section V reports the Legendre-moment analysis of the $d\Delta\sigma/d\Omega$ data, with the novel bootstrap-based fitting method used in the current analysis described in Sec. V A. The determination of the $E2/M1$ ratio from the definitions of the fitted Legendre-moments in terms of multipoles is reported in Sec. VI. Finally, the summary and outlook are given in Sec. VII.

II. EXPERIMENTAL SETUP

The helicity-dependent data used for this analysis were collected at the A2 tagged photon facility of the MAMI electron accelerator in Mainz, Germany [21].

Figure 1 shows a sketch of the A2 experimental setup used for the measurement. Since this setup has already been

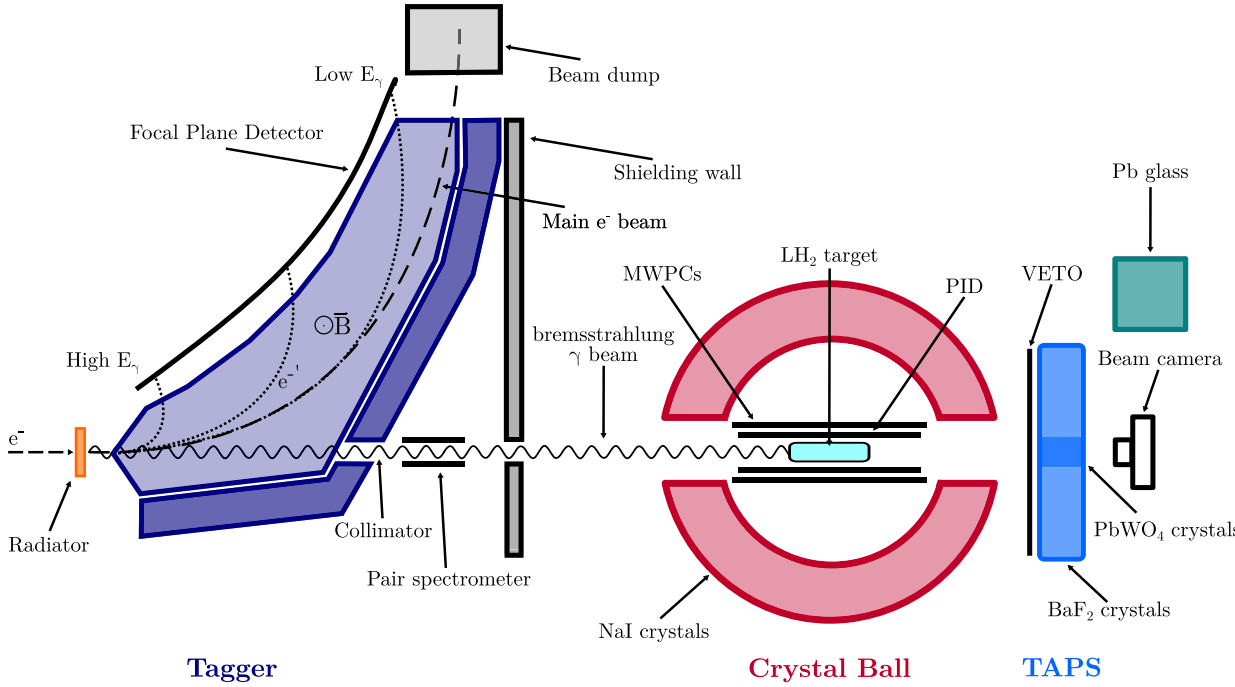

FIG. 1. Sketch of the experimental setup of the A2 Collaboration tagged photon facility, including photon tagging apparatus and detectors [22]. The figure is not to scale.

described in detail (see, for instance, Refs. [23–28] and references therein), we limit the discussion to the features relevant to the present experiment.

A. The photon beam

The circularly polarized photons used for this measurement were produced via Bremsstrahlung on an amorphous radiator of the 450-MeV longitudinally polarized electron beam. To avoid polarization-dependent photon flux values, the helicity of the electron beam was flipped at a rate of 1 Hz.

The electron polarization degree P_e was regularly determined by Mott scattering close to the electron source [29] and was found to be more than 80% with a systematic uncertainty of $\pm 3\%$.

The recoil electrons from the Bremsstrahlung process were momentum-analyzed using the Glasgow-Mainz spectrometer with an energy resolution of $\approx$1 MeV, corresponding to the width of the detector channels [30]. The resulting photon beam passed through a 2-mm-diameter lead collimator, reaching the target and detection apparatus.

The degree of the energy-dependent circular photon polarization $P_\odot^\gamma$ was determined using the Olsen and Maximon equation [31]:

$$\frac{P_\odot^\gamma}{P_e} = \frac{4x - x^2}{4 - 4x + 3x^2},$$

where $x = E_e/E_\gamma$, with E_e and E_γ being the energies of the electron and the Bremsstrahlung photon, respectively.

The photon tagging efficiency was measured once a day using a Pb-glass Cherenkov detector in dedicated low-flux runs. During the standard data-taking operation, fluctuations in the photon flux were monitored using a low-efficiency pair spectrometer located in the photon beamline after the collimator. An absolute systematic uncertainty in the photon flux of 4% was estimated by comparing the data from these detectors obtained under a range of different experimental conditions.

B. The target system

The longitudinally polarized proton target used in this experiment was the Mainz-Dubna Frozen Spin Target [32,33]. The filling factor for the $\simeq$2-mm-diameter butanol (C_4OH_{10}) spheres contained in the 2-cm-long, 2-cm-diameter target container was estimated to be 60%, with a systematic uncertainty of 2% [32].

The target material (butanol) was polarized using the dynamic nuclear polarization effect [34], which requires a high magnetic field (about 2.5 T) and a temperature of about 25 mK. A small holding magnetic field of 0.6 T, which replaced the polarizing magnet during the data-taking phase, allowed regular relaxation times of about 1000 h to be achieved.

The target polarization was measured with an NMR system before and after each data-taking period and then exponentially interpolated at intermediate times. Corrections to the calculated polarization values were necessary due to ice formation on the NMR coils. They were taken from Refs. [35,36], which independently analyzed the same data set used in the present work. Due to these corrections, as in Ref. [36], a conservative systematic uncertainty of 10% was applied to the target polarization values.

C. The hadron detector

The photon-induced reaction products were detected by the Crystal Ball-TAPS apparatus. The Crystal Ball (CB)

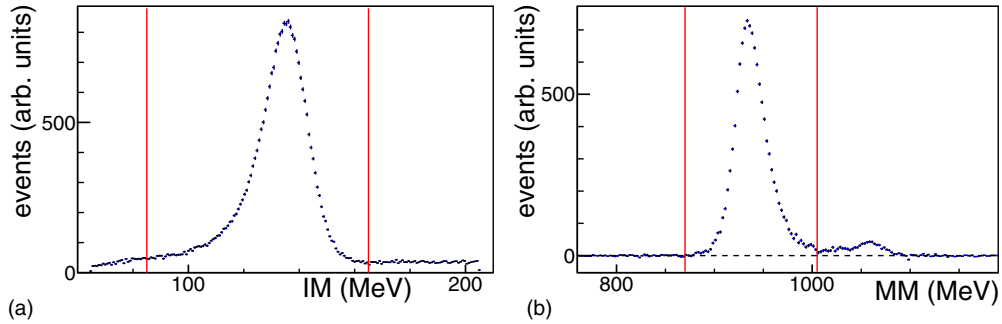

FIG. 2. (a) Two-photon invariant mass (IM) distribution from the π^0 reconstruction procedure obtained for the difference of the candidate events with the parallel and antiparallel spin configurations. (b) Same as before, but for the missing mass (MM) distribution after the IM-based selection shown in panel (a). In both cases, the acceptance region for the selection of a good $p\pi^0$ event is inside the vertical red lines.

calorimeter was placed around the target cell and covered the full azimuthal (ϕ) angle and a polar (θ) angle range from 21° to 159° [37]. It consisted of 672 NaI(Tl) crystals and had an ≈100% detection efficiency for photons coming from the π^0 decay. Inside the CB, from the inside out, there were a particle identification detector (PID), consisting of a barrel of 24 plastic scintillators, and two multiwire proportional chambers (MWPCs). The combination of all these detectors provided a precise tracking and identification of charged particles. The TAPS was a hexagonal wall covering the polar angle forward region outside the CB acceptance, $1^\circ < \theta < 20^\circ$, and was made of of 366 BaF_2 and 72 $PbWO_4$ crystals [38,39]. In front of each crystal there was a 5-mm-thick plastic scintillator (VETO) that was used for charged-particle identification. The combination of the large-acceptance CB and TAPS calorimeters covered ≈97% of the full solid angle.

III. DATA ANALYSIS

After offline energy and time calibration of all detectors, the data from the butanol target were analyzed, and all the implemented algorithms were tested and checked with simulation, to obtain an optimal identification of the $\gamma p \to p\pi^0$ channel.

No unpolarized background had to be evaluated since the effect of the C and O spinless nuclei present in the target vanishes in the $d\Delta\sigma/d\Omega$ difference [see Eq. (2)].

A. π^0 reconstruction and identification

The algorithms used for the data selection were basically the same as those described in Ref. [28]. Therefore, only a summary of the main analysis steps required to identify the $p\pi^0$ channel is given here.

The candidate events accepted for the differential cross-section evaluation were those with two neutral or three (with at least two neutral) clusters reconstructed inside the detector. A neutral cluster is defined as an energy deposition in one of the two calorimeters, without an associated hit in either the PID or the MWPC, or VETO for clusters in CB and TAPS, respectively.

Due to the relatively high tagged photon flux ($\approx 10^7$ γ/s), a time coincidence within 20 ns was required between the triggers in the calorimeters and the hits in the tagger focal plane detector. To remove the random coincidences in the selected time window, a side-band subtraction was also performed by selecting a background sample on each side of the prompt peak.

The first offline analysis step was the evaluation of the two-photon invariant mass (IM) using all neutral clusters of each event. For all events with more than two neutral hits, all possible combinations were used to calculate the IM and only the combination that gave the closest value to the nominal π^0 mass was retained for subsequent analysis steps.

The overall IM distribution obtained for the difference of candidate events with the parallel and antiparallel spin configurations is shown in Fig. 2(a), together with the cut (IM ∈ [85–165] MeV) applied in the offline analysis that selected the events for further analyses.

The next step was to evaluate the missing mass (MM) of the event, where the recoil nucleon of the reaction $\gamma N \to \pi^0 N$ was considered as a missing particle, even when it was detected. The missing mass was calculated as follows:

$$\mathrm{MM} = \sqrt{(E_\gamma + m_p - E_{\pi^0})^2 - (\vec{p}_\gamma - \vec{p}_{\pi^0})^2}, \qquad (3)$$

where E_γ and $\vec{p}_\gamma$ are the energy and momentum of the incoming photon in the laboratory frame, respectively, m_p is the proton mass in the initial state, and E_{π^0} and $\vec{p}_{\pi^0}$ are the reconstructed π^0 total energy and momentum, respectively.

The MM distribution obtained for the difference of candidate events after the previous analysis steps with the parallel and antiparallel spin configurations is shown in Fig. 2(b). Events from the $\pi^0\pi^0$ channel, coming from the high-energy part of the photon Bremsstrahlung spectrum, can be clearly seen as a small peak in the right part of the distribution. They are rejected by the applied selection cut (MM ∈ [870–1005] MeV) shown in Fig. 2(b).

To evaluate the residual contamination remaining after this cut, a sample of $\gamma p \to \pi^0\pi^0 p$ events was generated and their signal in the detection apparatus was simulated using a GEANT-based Monte Carlo code [40] that accurately modeled the geometry and composition of the detection apparatus and considered the applied electronic thresholds. This analysis showed that the fraction of the $\pi^0\pi^0$ events passing the MM

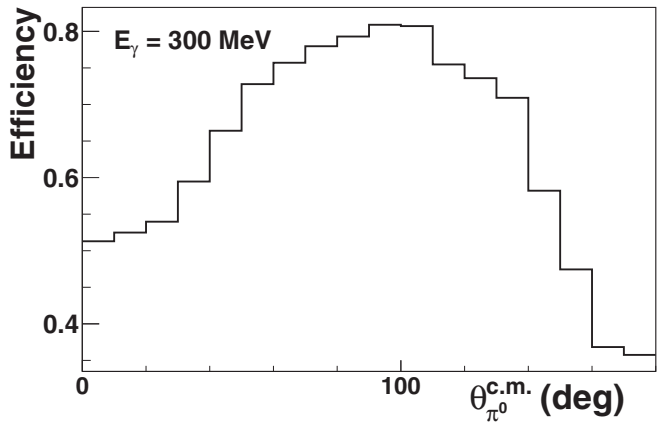

FIG. 3. π^0 reconstruction efficiency obtained using Monte Carlo simulated events at $E_\gamma = 300$ MeV, as a function of the polar π^0 emission angle in the c.m. system $\theta_{\pi^0}^{c.m.}$.

cut is about 2×10^{-3}. Therefore their contribution was completely neglected in the rest of the analysis.

The detection and reconstruction efficiency of the $p\pi^0$ events was also evaluated using the same GEANT-based code. As an example, the simulated π^0 reconstruction efficiency at the photon beam energy $E_\gamma = 300$ MeV is shown in Fig. 3 as a function the polar π^0 emission angle in the center-of-mass (c.m.) system ($\theta_{\pi^0}^{c.m.}$). This efficiency, over the full measured photon energy interval, varies in the forward, central, and backward angular regions within the ranges 40%–60%, 50%–90%, and 25%–50%, respectively.

TABLE I. Relative systematic uncertainties given as total widths of uniformlydistributed values.

Source	Error
Tagging efficiency	±4%
Beam polarization	±3%
Target polarization	±10%
Target density	±2%
π^0 reconstruction efficiency	±1%–7%

The relative systematic uncertainty was evaluated by examining the different cuts and selection conditions applied to both the experimental and the simulated data and it was estimated to be 10% of the value of the applied correction.

B. Systematic uncertainties

The various sources of systematic uncertainties discussed previously are summarized in Table I.

Sources of common constant systematic uncertainties come from the photon flux normalization, the beam and target polarization, and the target surface density. In contrast, the systematic uncertainty related to the π^0 reconstruction efficiency depends on both E_γ and $\theta_{\pi^0}^{c.m.}$ and ranges from ≈1% to ≈7% of the absolute $d\Delta\sigma/d\Omega$ values.

IV. RESULTS

A compact representation of the differential cross-section $d\Delta\sigma/d\Omega$ data can be obtained by plotting them as

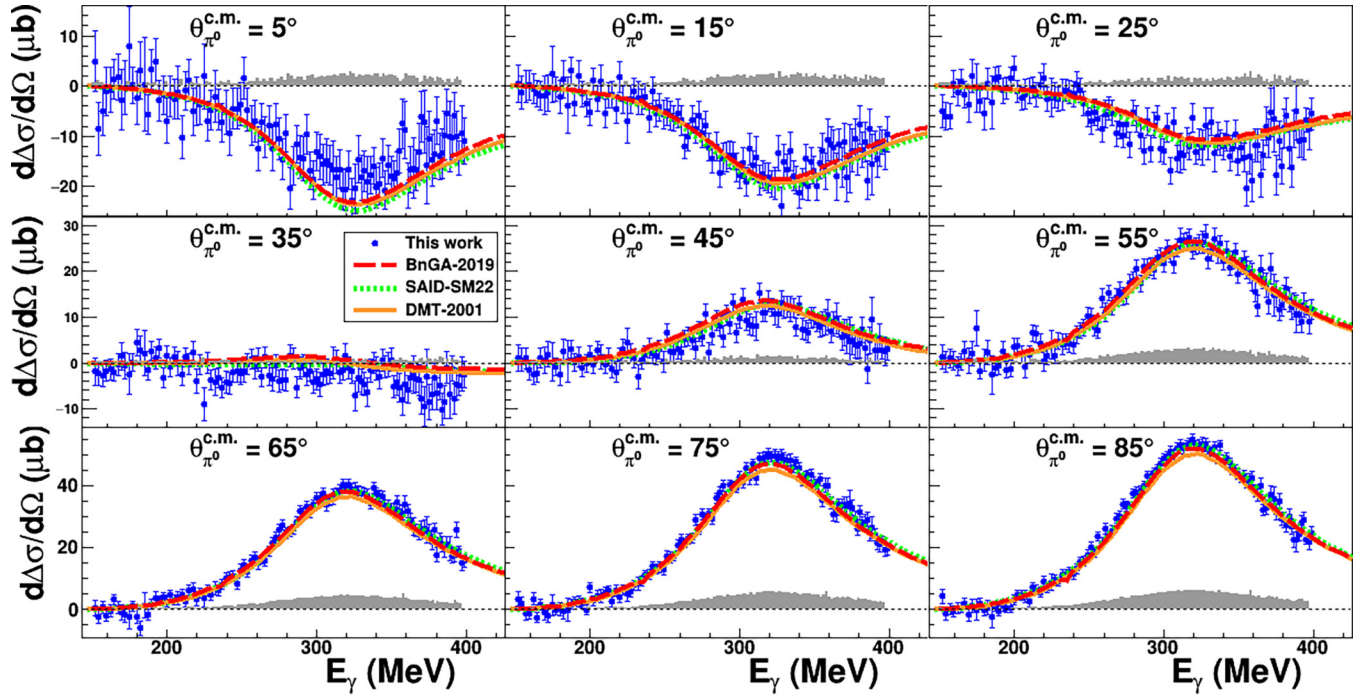

FIG. 4. Excitation functions of the $\vec{\gamma}\vec{p} \rightarrow p\pi^0$ reaction as a function of the photon beam energy for the measured forward $\theta_{\pi^0}^{c.m.}$ bins. The experimental results in blue are compared with the predictions given by the BnGa-2019 (dashed red lines) and SAID-SM22 (dotted green lines) energy-dependent PW analyses and by the DMT-2001 dynamical model (solid orange lines). The total contribution of all the systematic uncertainties, given in half-width units (see Sec. III B), is shown as gray bars.

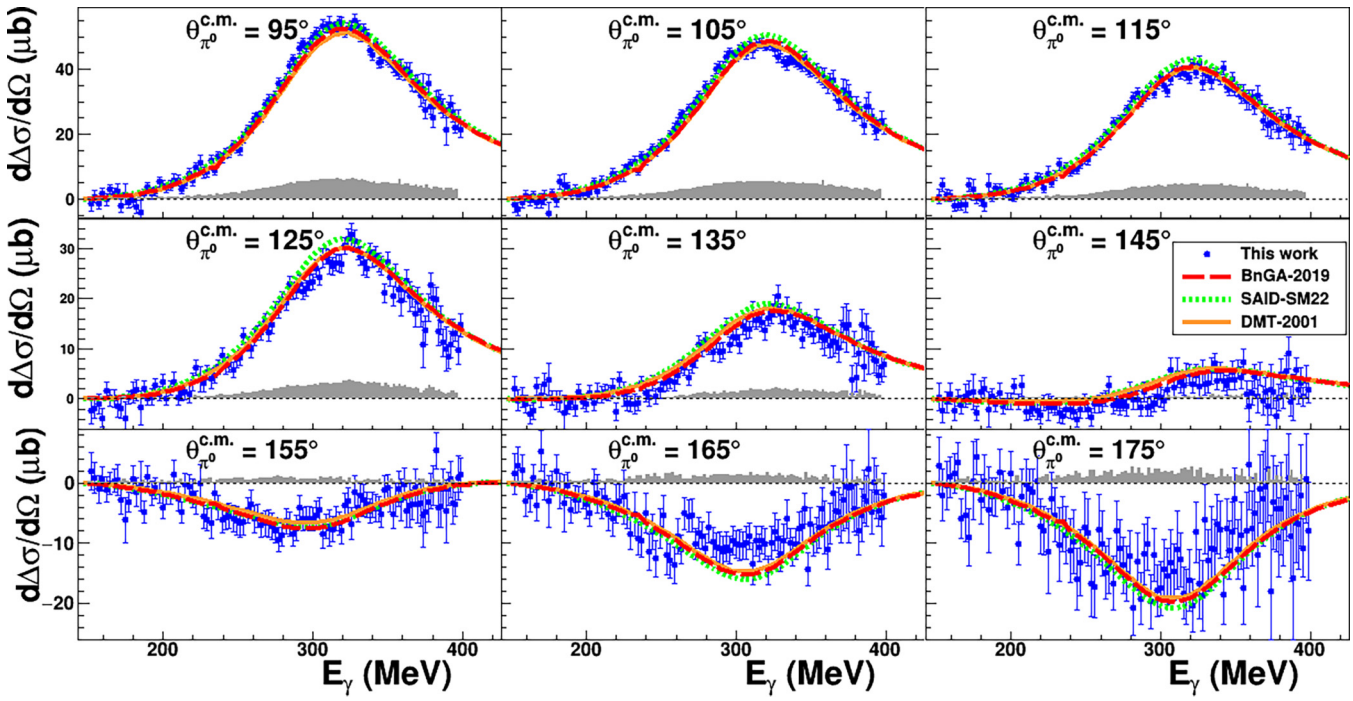

FIG. 5. Same as in Fig. 4, but for the measured backward $\theta^{\text{c.m.}}_{\pi^0}$ bins.

excitation functions at the measured $\theta^{\text{c.m.}}_{\pi^0}$ angles, as shown in Figs. 4 and 5.

The different lines show the predictions for this observable given by two energy-dependent partial wave (PW) analyses, BnGa-2019 [41] (dashed red lines) and SAID-SM22 [42] (dotted green lines), and by the DMT-2001 dynamical model [43–46] (solid orange lines). The DMT-2001 model is a field-theoretical meson-exchange model for πN scattering, optimized for the description of the single-pion photoproduction process below 400 MeV. In contrast to the previous PW analyses, the energy dependence of the DMT amplitudes is largely determined from theoretical considerations even though there are free parameters, describing the nonresonant part of the amplitudes, that are determined from the fit of $\gamma N \to \pi N$ data. In the comparison with our data, all the predictions show a rather good agreement in all energy ranges, except for slight differences at the very forward and backward angles.

In Fig. 6 some of the new $d\Delta\sigma/d\Omega$ data are compared, at fixed E_γ values, to all available results for this observable, which were published by the GDH [13] (red squares) and LEGS [47] (green up-triangles) Collaborations. As can be easily seen from the previous figures, the present work, with 18 (10° wide) $\theta^{\text{c.m.}}_{\pi^0}$ bins measured at 114 E_γ (≈2 MeV wide) bins, provides a huge improvement in both quantity and quality compared to the previous data in the $\Delta(1232)$ resonance region.

As a further check, Fig. 7 compares our results with a combination of previously published data from the A2 Collaboration (red down-triangles). These combined values were obtained, for $E_\gamma < 400$ MeV, by multiplying the unpolarized differential cross-section values $d\sigma_0/d\Omega$ from Ref. [48] with the recently published E asymmetry values from Ref. [49], according to the following well-known identity (see, for instance, Ref. [50]):

$$\frac{d\Delta\sigma}{d\Omega} = -2\frac{d\sigma_0}{d\Omega}E. \tag{4}$$

The excellent agreement found with both the previously published GDH and A2 data gives a strong indication of the overall correctness of the offline analysis procedures.

The total helicity-dependent cross section $\Delta\sigma$ for the $\gamma p \to p\pi^0$ reaction, obtained by integrating the differential cross section $d\Delta\sigma/d\Omega$ over the full solid angle, is shown in Fig. 8 (blue points) for the photon-beam energy range from $E_\gamma = 150$ MeV up to 400 MeV. It is again compared to the predictions given by the previous PW analyses and model and to the avaliable data from the GDH [13] (red points) and LEGS [47] (green points) Collaborations.

As already noticed for the excitation functions shown in Figs. 4 and 5, our data are in excellent agreement with the BnGa-2019 and SAID-SM22 PW analyses, the DMT-2001 model, and the GDH data, while differing from the LEGS data in the region around the Δ resonance mass. As can be clearly deduced from the differential cross-section data shown in Fig. 6, this discrepancy comes from differences in the angular shape, especially present in the forward $\theta^{\text{c.m.}}_{\pi^0}$ region, that cannot be accommodated with a single common scale shift.

V. LEGENDRE ANALYSIS OF THE $d\Delta\sigma/d\Omega$ DATA

The multipole content of the reaction amplitude can be easily accessed by expanding the measured $d\Delta\sigma/d\Omega$ angular distributions in a (truncated) Legendre series.

The energy dependence of the expansion coefficients can reveal specific correlations between individual resonance states of certain parities (see, for instance, Ref. [50] and

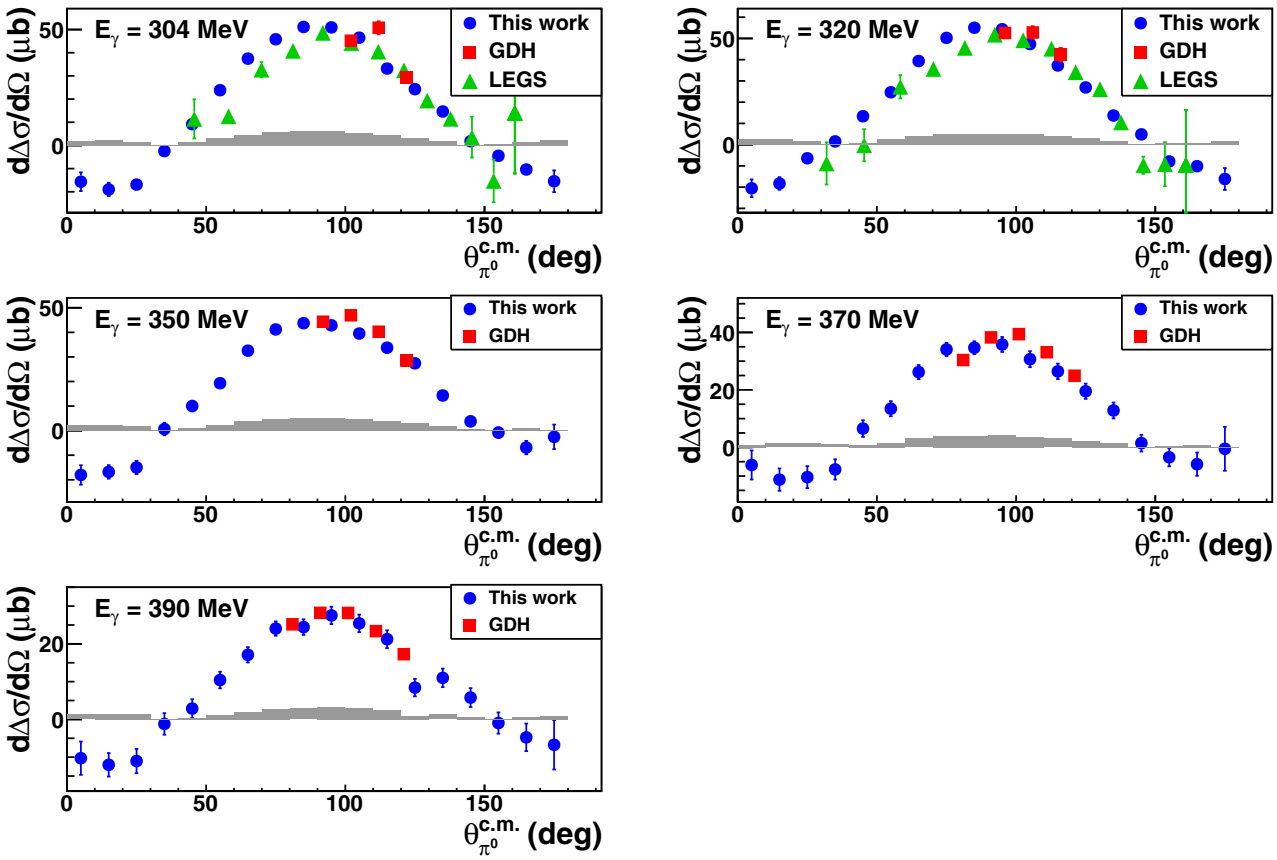

FIG. 6. The new data on the differential helicity-dependent cross section (blue circles) are compared with available published data from the GDH [13] (red squares) and LEGS [47] (green up-triangles) Collaborations. The total contribution of the systematic uncertainties of the present data, given in half-width units (see Sec. III B), is shown as gray bars.

references therein). This method proved to be particularly effective for $E_\gamma < 400$ MeV, where only one well-known resonance, $\Delta(1232)$, dominates the amplitude and low-lying multipoles can be accessed via the interference terms with the dominant M_{1+} term.

The Legendre coefficients a_k were then obtained by fitting a series of associated Legendre polynomials P_k to the angular distributions $d\Delta\sigma/d\Omega$ with the following function (see Ref. [50]):

$$\frac{d\Delta\sigma}{d\Omega} = -2\,\frac{q}{k}\sum_{k=0}^{2\ell_{\max}} \left(a_{\ell_{\max}}\right)_k (W) P_k(\cos\theta), \tag{5}$$

where q, k, and W are the photon and π^0 momenta and the total energy in the c.m. system, respectively. The notation $(a_{\ell_{\max}})_k$ means that in the fitting procedure only the partial waves with the πN relative angular momentum up to $\ell = \ell_{\max}$ were included in the fit. The multipoles contributing to the fit for $\ell_{\max} = 1$ and 2 are listed in Table II.

A. Bootstrap-based fitting procedure

As noted in Ref. [50], an important issue when using this type of algorithm is the proper handling of the systematic uncertainties associated with the data being fit. A widely used method, when one single common and Gaussian-distributed multiplicative systematic uncertainty is present, is to introduce a modified χ^2 function, with an additional overall scale parameter to be fitted (see, for instance, Refs. [51,52]):

$$\chi^2_{\rm mod}(\vartheta) = \sum_i \left(\frac{f y_i - T_i(\vartheta)}{f\sigma_i}\right)^2 + \left(\frac{f-1}{\sigma_{\rm sys}}\right)^2. \tag{6}$$

Here y_i and σ_i are the experimental values to be fitted and their corresponding statistical uncertainties in root-mean-square units (rms), respectively. T_i are the theoretical predictions given by a model depending on the set of unknown parameters ϑ to be evaluated from the data, and f and $\sigma_{\rm sys}$ are the additional fit parameter and its estimated uncertainty (in rms units), respectively.

However, Eq. (6) cannot be used to fit the new $d\Delta\sigma/d\Omega$ data, since they have both uniform and angular-dependent systematic uncertainties, as discussed in Sec. III B, and these effects cannot be properly accounted for by the single factor f. Moreover, under these conditions, the goodness-of-fit distribution is generally not given by the χ^2 function

TABLE II. The multipole amplitudes contributing to the fitted cross section reported in Eq. (5) for different choices of $\ell_{\max}$.

$\ell_{\max}$	Wave	Multipole
1	s wave	E_{0+}
	p wave	E_{1+}, M_{1+}, M_{1-}
2	d wave	$E_{2+}, E_{2-}, M_{2+}, M_{2-}$

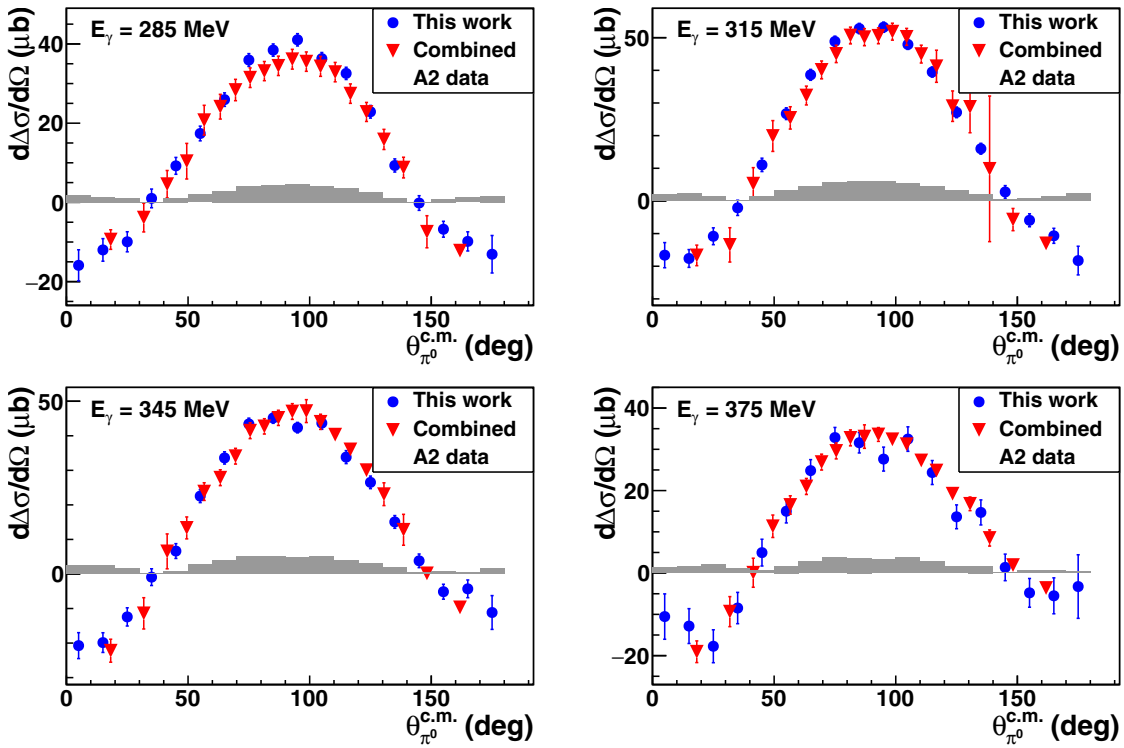

FIG. 7. The new data on the differential helicity-dependent cross section (blue circles) are compared to a combination of previously published A2 data [48,49] (red down-triangles). See text for details. The total contribution of the systematic uncertainties of the present data, given in half-width units (see Sec. III B), is shown as gray bars.

and the fit parameter errors are not *a priori* Gaussian, since the sum appearing in Eq. (6) consists of correlated and non-Gaussian variables.

To overcome all these difficulties, the fit to the present data was performed by using an innovative method [52], based on the parametric bootstrap technique, already successfully deployed for different analyses of nuclear Compton scattering data (see Refs. [53–55]).

As an example, in the case of a single data set with Gaussian statistical errors and uniform common multiplicative systematic uncertainties, this method consists of randomly generating N Monte Carlo replicas of the experimental data, where each data point y_i is replaced by

$$y_i \to y_i^{(b)} = (1 + \delta_b)(y_i + r_{i,b}\sigma_i).$$

The indices i and b run over the number of data points and the bootstrap replica, respectively; $r_{i,b}$ is a random number

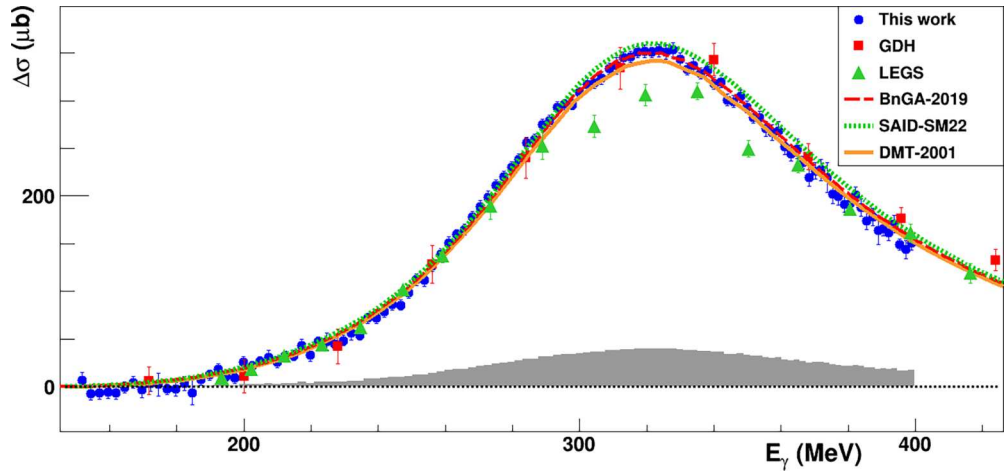

FIG. 8. The new total helicity-dependent cross section $\Delta\sigma$ for the $\gamma p \to p\pi^0$ channel (blue circles) is compared with the results obtained by the GDH [13] (red squares) and LEGS [47] (green up-triangles) Collaborations. The different line styles show the predictions of the BnGa-2019 [41] (dashed red line) and SAID-SM22 [42] (green dotted line) PW analyses and of the DMT-2001 dynamical model [43–46] (solid orange line). The total contribution of the systematic uncertainties, given in half-width units (see Sec. III B), is shown as gray bars.

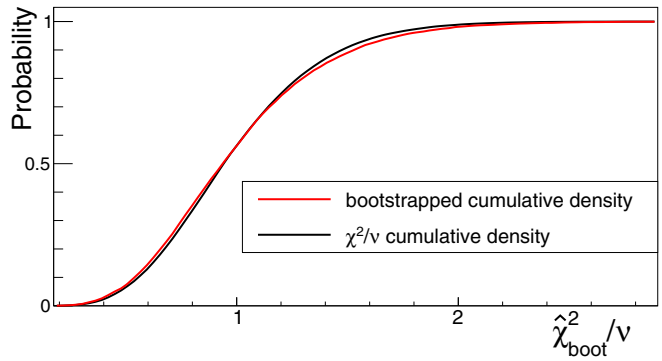

FIG. 9. The cumulative density function (CDF) of the goodness-of-fit distribution divided by the number of degrees of freedom (ν), as obtained from the bootstrap procedure (red solid line) at $E_\gamma = 350$ MeV, is compared with the CDF of the reduced χ^2 distribution (black solid line).

extracted from the normal distribution $\mathcal{N}(0, 1)$, and δ_b is a uniform random variable distributed according to $\mathcal{U}[-\Delta, \Delta]$, where $\pm\Delta$ is the quoted systematic uncertainty interval. A set of fitted parameters ($\boldsymbol{\vartheta}_b$) is extracted from each of the N simulated replicas and, at the end of the procedure, the best values ($\hat{\boldsymbol{\vartheta}}_{\rm boot}$) and the errors of the fitted quantities can be easily extracted from the empirical statistical parameters of the resulting distributions.

The goodness of fit (see again Ref. [52]) is evaluated by comparing the minimum $\hat{\chi}^2_{\rm boot}$ value obtained as

$$\hat{\chi}^2_{\rm boot} = \sum_i \left(\frac{y_i - T_i(\hat{\boldsymbol{\vartheta}}_{\rm boot})}{\sigma_i} \right)^2, \tag{7}$$

with the theoretical distribution empirically obtained by repeating the bootstrapping algorithm with each experimental datum y_i replaced by $T_i(\hat{\boldsymbol{\vartheta}}_{\rm boot})$. With this procedure, after a suitably large number k of bootstrap cycles, an estimate of the goodness-of-fit probability function can be obtained from the set of minimum values

$$\hat{\chi}^2_{\rm th,boot,1}, \hat{\chi}^2_{\rm th,boot,2}, \ldots, \hat{\chi}^2_{\rm th,boot,k}$$

evaluated at the end of each cycle. This ensures that the correct p value is then always provided by the present fitting procedure.

B. Fit results

A total of $N = 10^4$ bootstrap samples were generated for each W bin, and the minimization was performed at the end of each iteration.

All the different systematic uncertainties were assumed to follow a uniform distribution over the interval defined by the bounds given in Table I. In the case of the angular-dependent source, the same common fraction of the full variation interval was randomly generated, for all angular bins, at each bootstrap cycle. The final total uncertainty factor entered into the bootstrap procedure is given by the product of all the random uniform variables generated by the previous procedure.

First, we evaluated the expected goodness-of-fit distribution, from which the p value associated with the minimum $\hat{\chi}^2_{\rm boot}$ values obtained by the bootstrap procedure has to be computed. Figure 9 shows the obtained cumulative density function (CDF) divided by the number of degrees of freedom (ν), obtained at $W = 1240$ MeV ($E_\gamma = 350$ MeV) and with $\ell_{\rm max} = 1$, compared with the CDF of the reduced χ^2 distribution. These two distributions were found to basically coincide, and the same result was obtained for all W bins as well as for $\ell_{\rm max} = 2$.

In the second step of this procedure, we evaluated the minimum value of the $\ell_{\rm max}$ parameter that could reproduce sufficiently well the behavior of the experimental data. This was done by comparing, at each W bin, the $\hat{\chi}^2_{\rm boot}$ values obtained for both $\ell_{\rm max} = 1$ and $\ell_{\rm max} = 2$ after a simultaneous fit of all the involved coefficients, as shown in Fig. 10.

Except for a few points in the center-of-mass energy region $W \approx 1200$ MeV, the fit with $\ell_{\rm max} = 2$ gives, in general, no significant improvement in the $\hat{\chi}^2_{\rm boot}$ values. In several cases where the difference is significant, the $\hat{\chi}^2_{\rm boot}$ values obtained with $\ell_{\rm max} = 2$ are suspiciously low values, which may indicate overfitting.

In addition, for $\ell_{\rm max} = 1$, we have that, after averaging over all W bins, $\langle \hat{\chi}^2_{\rm boot}/\nu \rangle = 1.14$, which corresponds to a p value of about 31%. All previous indications lead us to conclude that the fit with $\ell_{\rm max} = 1$ reproduces our data sufficiently well. Such a result was to be expected since, in the $\Delta(1232)$ region, the production of s- and p-wave pions gives, by far, the largest contribution to the π^0 channel, while d waves only contribute thanks to very small interference terms with the dominant p waves. Their effect can be quantified by the value of the $(a_2)_3$ Legendre coefficient calculated with the previous PW analyses and model. In the $\Delta(1232)$ region, the absolute value of this coefficient was found to be $\lesssim 1$ μb/sr, more than 1 order of magnitude smaller than the absolute contributions given by the $(a_1)_0$ and $(a_1)_2$ coefficients, dominated by the p-wave multipoles, and also at least 2 times lower than the $(a_1)_1$ coefficient, which quantifies the small s-p interference contribution (see Fig. 12). Contributions due to d-wave pions can then be safely neglected in the present context.

An example of the probability distributions for the fit parameters $(a_1)^b_0$, $(a_1)^b_1$, and $(a_1)^b_2$, computed at the end of each bootstrap replica, is given in Fig. 11, where these densities are plotted at $W = 1240$ MeV ($E_\gamma = 350$ MeV). For the reasons discussed earlier, these distributions, especially for the $(a_1)^b_0$ and $(a_1)^b_2$ parameters, show significant deviations from the pure Gaussian shape, as indicated by the comparison with the best-fit Gaussian red curves. Very similar density functions were found for all other W bins.

The values of the Legendre coefficients $(a_1)_0$, $(a_1)_1$, and $(a_1)_2$, determined as the mean of distributions obtained by the bootstrap-based fit procedure at each W bin, are plotted in Fig. 12. The quoted fit errors are the 68% confidence level (CL) determined using the quantiles of the bootstrapped parameter distributions and include the contribution of both the statistical and systematic uncertainties of the experimental data. The numerical values of all these coefficients are reported in Tables III to V in the Appendix.

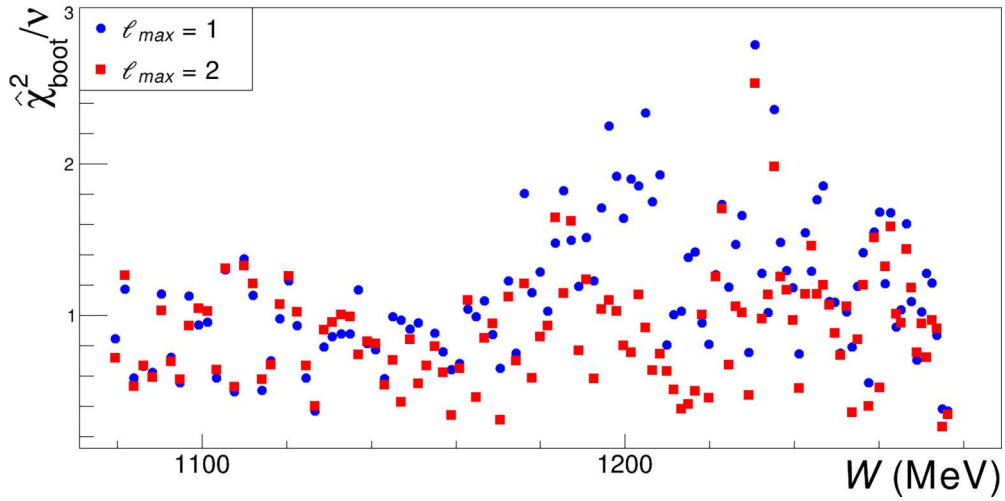

FIG. 10. Reduced $\hat{\chi}^2$ values obtained from the bootstrap procedure, as a function of the center-of-mass energy W at $\ell_{\max} = 1$ (blue circles) and $\ell_{\max} = 2$ (red squares).

The different curves represent the corresponding coefficients evaluated with the BnGa-2019 and SAID-SM22 PW analyses with the DMT-2001 dynamical model. A quite good agreement is found with all the previous predictions for the $(a_1)_0$ and $(a_1)_2$ coefficients, whose value is mostly determined by the dominant p-wave contributions ([see later Eqs. (8) and (9). On the contrary, these predictions give sizable differences in the value of the $(a_1)_1$ coefficient, which quantifies the effects of the s-p interference terms. Our new data will allow to resolve these discrepancies and improve our understanding of the role of the low-lying multipoles for the πN process in the $\Delta(1232)$ energy region.

VI. DERIVATION OF THE $E2/M1$ RATIO

In the $\ell_{\max} = 1$ approximation (i.e., only s and p waves are considered—see Table II), the Legendre coefficients of the helicity-dependent differential cross section can be decomposed in terms of multipoles as [50,56]

$$\begin{aligned}(a_1)_0 &= |E_{0+}|^2 + |M_{1-}|^2 + 3E^*_{1+}(3E_{1+} + M_{1+}) \\ &\quad + M^*_{1+}(3E_{1+} - M_{1+}), \\ (a_1)_1 &= E^*_{0+}(3E_{1+} - M_{1-} + M_{1+}) \\ &\quad + E_{0+}(3E^*_{1+} - M^*_{1-} + M^*_{1+}), \\ (a_1)_2 &= -M^*_{1-}(3E_{1+} + M_{1+}) + E^*_{1+}(6E_{1+} - 3M_{1-}) \\ &\quad - M^*_{1+}(M_{1-} - 2M_{1+}). \end{aligned} \tag{8}$$

To evaluate R_{EM} [see Eq. (1)] from these equations, the following two approximations were sequentially applied:

(i) all terms involving only the E_{0+}, E_{1+}, and M_{1-} multipoles were dropped as, in the region of the $\Delta(1232)$ resonance mass, they can be assumed to be negligible compared to the terms where M_{1+} contributes;

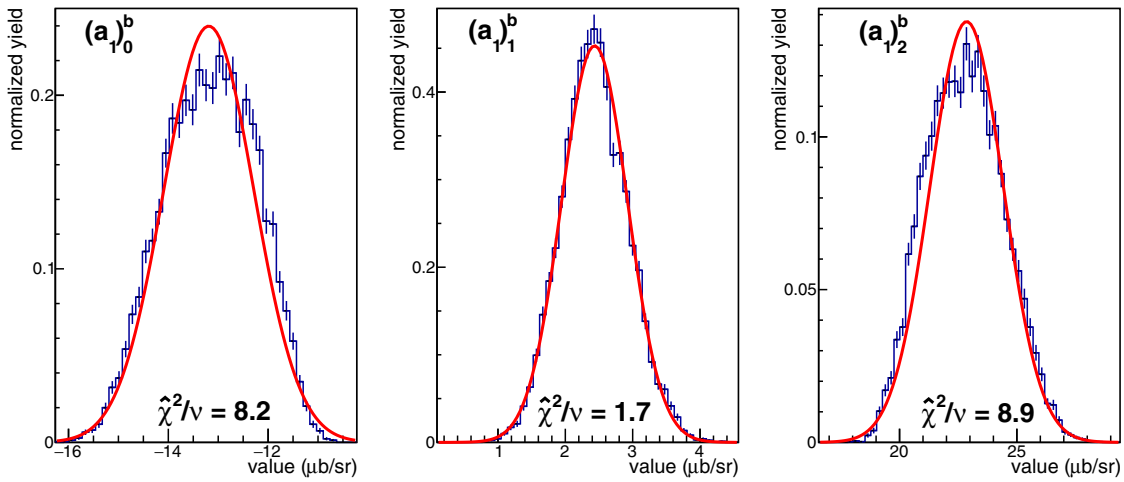

FIG. 11. Probability distributions for the fit parameters $(a_1)^b_0$, $(a_1)^b_1$, and $(a_1)^b_2$ as determined at the end of each bootstrap replica at $W = 1240$ MeV ($E_\gamma = 350$ MeV). These distributions are compared with the best-fit Gaussian curves (red lines), and the corresponding $\hat{\chi}^2/\nu$ values are also given at the bottom of each plot.

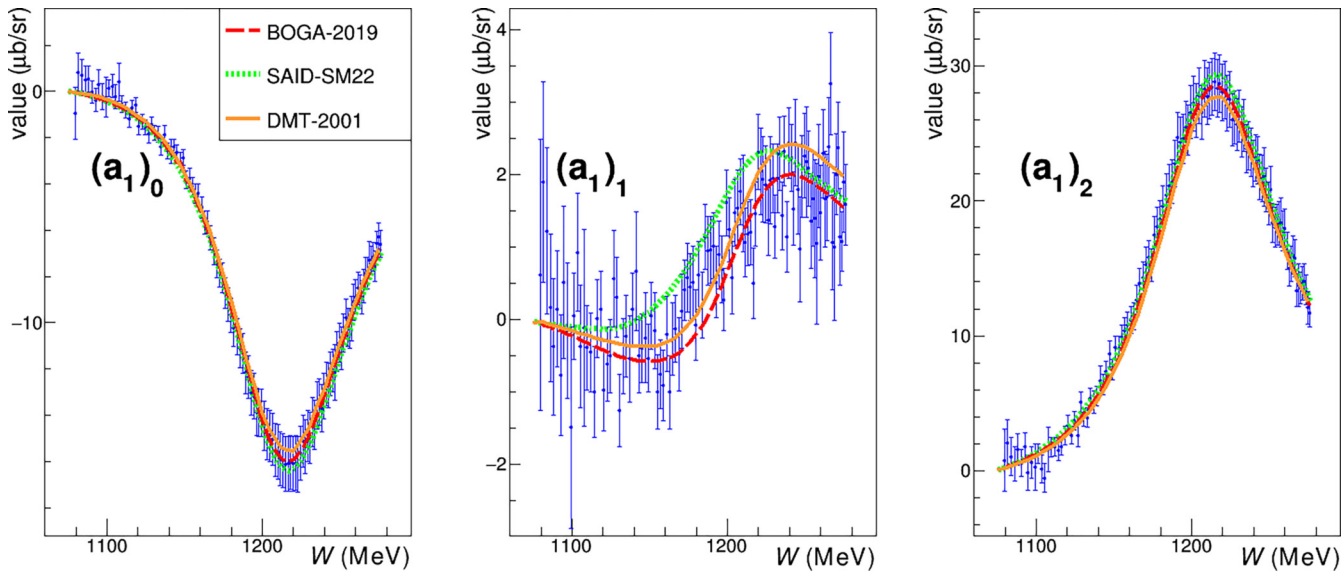

FIG. 12. The fitted Legendre coefficients $(a_1)_0$, $(a_1)_1$, and $(a_1)_2$ are compared with the predictions of the BnGa-2019 [41] (dashed red lines) and SAID-SM22 [42] (dotted green lines) PW analyses and of the DMT-2001 dynamical model [43–46] (solid orange lines).

(ii) a perfect Breit-Wigner form was assumed for the M_{1+} multipole, which gives, by far, the largest contribution to the $\Delta(1232)$ resonance excitation. Under this assumption, the real part of the M_{1+} multipole vanishes exactly at the M_Δ value. We can therefore set

$$M_{1+} \simeq i\mathrm{Im}[M_{1+}].$$

The first step in deriving R_{EM} was to apply approximation (i) to the coefficients given in Eq. (8):

$$\begin{aligned}(a_1)_0 &\simeq -|M_{1+}|^2 + 3E_{1+}^* M_{1+} + 3M_{1+}^* E_{1+} \\ &= -|M_{1+}|^2 + 6\mathrm{Re}[E_{1+}^* M_{1+}], \\ (a_1)_1 &\simeq 2\mathrm{Re}[E_{0+}^* M_{1+}], \\ (a_1)_2 &\simeq -2\mathrm{Re}[M_{1-}^* M_{1+}] + 2|M_{1+}|^2. \end{aligned} \tag{9}$$

It can be immediately noticed that the coefficient $(a_1)_1$ is irrelevant for further considerations and is ignored from now on. Furthermore, applying approximation (ii) resulted in

$$\begin{aligned}(a_1)_0 &\simeq -\mathrm{Im}[M_{1+}]^2 + 6\mathrm{Im}[E_{1+}]\mathrm{Im}[M_{1+}], \\ (a_1)_2 &\simeq 2\mathrm{Im}[M_{1+}]^2 - 2\mathrm{Im}[M_{1-}]\mathrm{Im}[M_{1+}] \simeq 2\mathrm{Im}[M_{1+}]^2, \end{aligned} \tag{10}$$

where, in the last step of the previous equation, it was considered that $\mathrm{Im}[M_{1-}] \ll \mathrm{Im}[M_{1+}]$ around the M_Δ value.

Using Eq. (10), and recalling Eq. (1), the ratio $(a_1)_0/(a_1)_2$ can now be calculated as

$$\frac{(a_1)_0}{(a_1)_2} \simeq -\frac{\mathrm{Im}[M_{1+}]^2}{2\mathrm{Im}[M_{1+}]^2} + \frac{6\mathrm{Im}[E_{1+}]\mathrm{Im}[M_{1+}]}{2\mathrm{Im}[M_{1+}]^2} = 3R_{EM} - \frac{1}{2}. \tag{11}$$

The following quantity can then be defined as a suitable approximation for R_{EM}:

$$R_L = \frac{1}{3}\frac{(a_1)_0}{(a_1)_2} + \frac{1}{6} \simeq R_{EM}. \tag{12}$$

This allows for the extraction of the parameter R_L from the ratio of only two Legendre coefficients fitted from the angular distribution of only one observable, $d\Delta\sigma/d\Omega$. This procedure has two main advantages: (i) it reduces by 1 the number of experimental observables to be measured compared to some of the previous extractions (e.g., Ref. [15]); and (ii) the experimental uncertainty of R_L is independent of all common scaling systematic uncertainties affecting the experimental data, as previously noted in Ref. [14].

The probability distribution for the parameter R_L^b obtained by the bootstrap procedure at $W = 1240$ MeV ($E_\gamma = 350$ MeV) is shown in Fig. 13(a). As can be seen from the result of the fit, this distribution can be considered approximately Gaussian, even though it is given by the ratio of two non-Gaussian variables.

In Fig. 13(a), R_L is plotted as a function of the center-of-mass energy W for the upper part of the measured photon-energy interval. The quoted fit errors are the 68% C.L. and include the contribution of both the statistical and angular-dependent systematic uncertainties of the experimental data.

In the same figure, the W dependence of the ratio,

$$R_W = \frac{\mathrm{Im}\left[E_{1+}^{3/2}\right]}{\mathrm{Im}\left[M_{1+}^{3/2}\right]}, \tag{13}$$

as predicted by BOGA-2019, SAID-SM22, and DMT-2001, is also shown. For all the different predictions, R_W is strongly dependent on the W value, while the experimental R_L values show quite small variations around the M_Δ value.

In order to give an estimate of R_{EM} from the distribution of R_L, a small center-of-mass energy interval $W = 1232 \pm 10$ MeV was then chosen, and the weighted average of all R values included in this interval was evaluated. This interval is centered around the M_Δ value, where R_L can be considered constant and the approximated Eq. (11) holds. The model systematic uncertainty associated with the approximations that led to Eq. (12) was evaluated, using the multipoles from

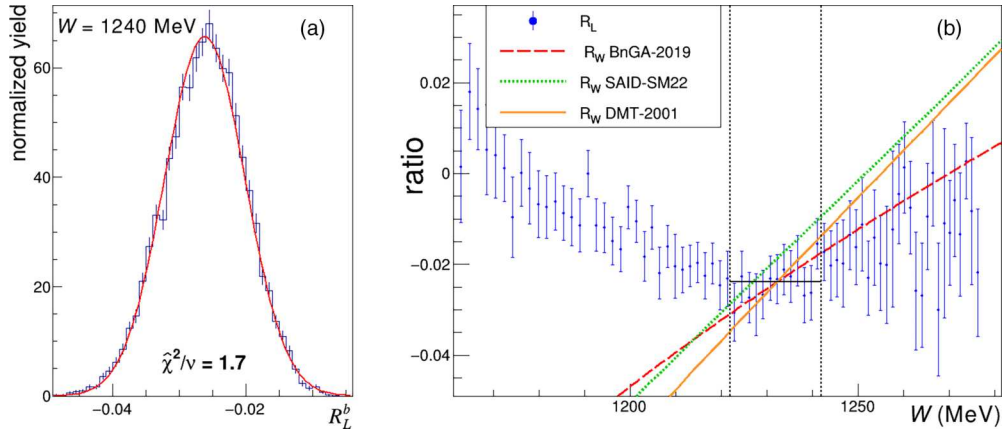

FIG. 13. (a) Probability distribution for the R_b parameter [see Eq. (12)], as determined by the bootstrap procedure at $W = 1240$ MeV ($E_\gamma = 350$ MeV). This distribution is compared to the best-fit Gaussian curves (red lines), and the corresponding $\hat{\chi}^2/\nu$ value is also given in the canvas. (b) The W (total c.m. energy) dependence of R_L [see Eq. (12)] for the upper part of the measured photon-energy interval is compared to the R_W ratio [see Eq. (13)] predicted by BOGA-2019 (dashed red line), SAID-SM22 (dotted green line) and DMT-2001 (solid orange line). The vertical dotted black lines define the W region 1232 ± 10 MeV selected to evaluate R_{EM}, while the horizontal black segment is drawn at $R = -0.0238$.

both the previous PW analyses and the DMT-2001 model, by comparing the exact R_{EM} value obtained with Eq. (1) with the average of the R values calculated with the approximated formula of Eq. (12) in the interval $W = 1232 \pm 10$ MeV. The maximum relative deviation between these two estimates was found to be 4%.

A 30% variation in the width of the selected interval resulted in a ≈4% change in both the evaluated R_{EM} value and its model systematic uncertainty. We then conservatively assume that the overall relative systematic uncertainty associated with both the model approximation and the interval choice is ±4% in rms units.

Finally, our new estimate of the parameter R_{EM} is then

$$R_{EM} = [-2.38 \pm 0.16(\text{stat.} + \text{sys.}) \pm 0.10(\text{model})]\%. \quad (14)$$

In Fig. 14, the newly evaluated R_{EM} value is compared to other recently published extractions given by the DAPHNE [14], LARA [16], LEGS [5], TAPS [15], and GDH [13] Col-

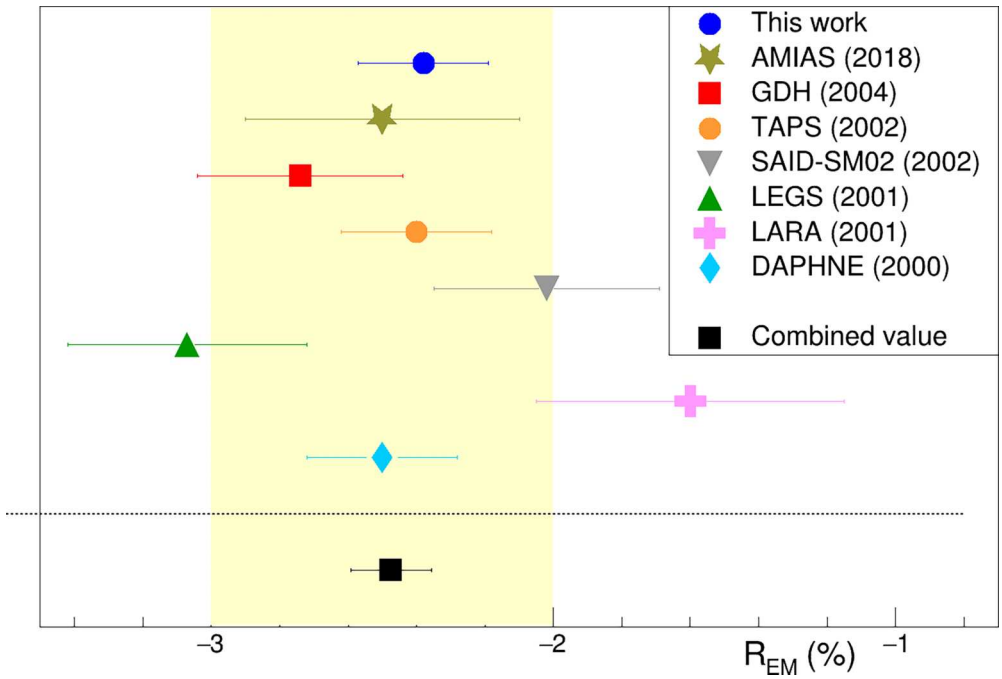

FIG. 14. The R_{EM} value obtained in this work (blue circle) is compared to the most recent evaluations from Ref. [18] (AMIAS, olive yellow star), Ref. [13] (GDH, red square), Ref. [15] (TAPS, orange circle), Ref. [57] (SAID-SM02. gray down-triangle), Ref. [5] (LEGS, green up-triangle), Ref. [16] (LARA, pink cross), and Ref. [14] (DAPHNE, cyan diamond). All quoted errors are the sum of both statistical, systematic, and model-dependent uncertainties. The vertical yellow band indicates the 100% CL interval estimated by the PDG [17]. The black square below the dotted line is the newly calculated weighted average R_{EM}^{AV}, using some of the previous results (see text for details).

laborations, by the SAID-SM02 PW analysis [57], and by the AMIAS [18] calculation. In this last approach, the $\gamma N \rightarrow N\pi$ reactions were described using the multipole expansions of the Chew-Goldberger-Low-Nambu (CGLN) amplitudes (see Ref. [58]). A random set of multipole coefficients was then generated by taking into account the allowed physical limits and the required constraints. The predictions for the different observables given by each set of coefficients were finally compared to the selected $\gamma N \rightarrow N\pi$ experimental data set (see Ref. [18]) and the final result and its uncertainty were evaluated from the obtained χ^2 probability values.

The value of the systematic uncertainty associated with the SAID-SM02 PW analysis ($\pm 3\%$) was taken from the work of the BRAG Group [59] that performed different multipole analyses using a common data base to gauge the model-dependence of such fits.

The present work provides an estimate with uncertainties that are not only more favorable, but also more rigorously calculated compared to previous work.

Within the quoted errors, there is a good agreement between all the different evaluations. For this reason, it is possible to combine them to obtain the most accurate extraction of R_{EM} available, which should be used for any further reference and for model comparison.

For this estimate, we did not include data from the LEGS [5] Collaboration because, as the authors themselves stated in their original publication, a part of the data set from the $\gamma p \rightarrow N\pi$ reactions used for their evaluation is not consistent with the data sets obtained at MAMI (see also Refs. [4,13–15]). Similarly, we have also not included the R_{EM} value from the LARA Collaboration [16] since their proton Compton-scattering data give inconsistent results when compared to all other available data for this reaction (see Ref. [55]).

Our new evaluation was then calculated by combining the present value with those from Refs. [13–15], all based on independent data sets. The weighted average of the selected values is

$$R_{EM}^{\mathrm{AV}} = [-2.47 \pm 0.12(\mathrm{stat.} + \mathrm{sys.} + \mathrm{mod.})]\%, \qquad (15)$$

where the quoted error is the sum of the statistical, systematic, and model-dependent errors.

VII. SUMMARY AND CONCLUSIONS

New precise data on the helicity-dependent differential cross section of single π^0 photoproduction on the proton have been obtained. Compared to the existing data, this new measurement covers a much larger energy and polar angular interval with a significantly improved precision. These new data improve our understanding of the $p\pi^0$ photoproduction process in the $\Delta(1232)$ energy region and, in particular, of the role of the low-lying multipoles, whose predicted contribution differs significantly between the available PW analyses and models.

From a Legendre moment analysis of the obtained angular distributions, the ratio $R_{EM} = (-2.38 \pm 0.16 \pm 0.10)\%$ at the $\Delta(1232)$ resonance mass value was obtained. This is the most accurate estimate from one single experiment ever published until now.

By combining some of the available estimates, the most accurate experimental R_{EM} value has been determined to be $R_{EM}^{AV} = (-2.47 \pm 0.12)\%$, where the quoted error is the sum of statistical, systematic, and model-dependent errors. This value should be used for all further reference and model comparisons.

ACKNOWLEDGMENTS

The authors wish to acknowledge the excellent support of the accelerator group of MAMI. This work was supported by SchweizerischerNationalfonds (Grants No. 200020-156983, No. 132799, No. 121781, and No. 117601); Deutsche Forschungsgemeinschaft (Grants No. SFB443, No. SFB1044, No. SFB/TR16, and No. FOR5327); the INFN-Italy; the European Community-Research Infrastructure Activity under the FP7 programme (Hadron Physics, Grant Agreement No. 227431); the U.K. Science and Technology Facilities Council under Grants No. ST/J000175/1, No. ST/G008604/1, No. ST/G008582/1, No. ST/J00006X/1, No. ST/V001035/1ST/V002570/1, No. ST/P004385/2, No. ST/T002077/1, and No. ST/L00478X/2; and the Natural Sciences and Engineering Research Council (NSERC, Grant No. FRN:SAPPJ-2015-00023), Canada. This material is based upon work also supported by the U.S. Department of Energy, Office of Science, Office of Nuclear Physics Research Division, under Awards No. DE-FG02-99ER41110, No. DE-FG02-88ER40415, No. DE-FG02-01-ER41194, No. DE-SC0014323, and No. DE-SC0016583, and by the National Science Foundation, under Grants No. PHY-1039130 and No. IIA-1358175.

APPENDIX

The numerical values of all the fitted legendre coefficients $(a_1)_0$, $(a_1)_1$, $(a_1)_2$ are reported in Tables III, IV, and V as a function of the total-center-of-mass energy W.

TABLE III. Numerical values of the fitted Legendre coeffcients $(a_1)_0$, $(a_1)_1$, $(a_1)_2$ in the total center-of-mass energy range 1079.5 MeV $\leqslant W \leqslant$ 1162.8 MeV. The quoted fit errors are the 68% confidence level determined using the quantiles of the bootstrapped parameter distributions and include the contribution of both the statistical and systematic uncertainties of the experimental data.

W (MeV)	$(a_1)_0$ (μb/sr)	$(a_1)_1$ (μb/sr)	$(a_1)_2$ (μb/sr)
1079.5	-1.0 ± 1.1	0.6 ± 1.9	0.8 ± 2.3
1081.7	0.8 ± 0.8	1.9 ± 1.4	2.0 ± 1.7
1083.9	0.7 ± 0.7	1.2 ± 1.2	1.0 ± 1.4
1086.1	0.5 ± 0.6	0.2 ± 1.0	0.5 ± 1.3
1088.3	0.5 ± 0.6	-0.4 ± 0.9	1.6 ± 1.2
1090.5	-0.0 ± 0.5	0.1 ± 0.8	0.6 ± 1.0
1092.6	-0.4 ± 0.5	-0.8 ± 0.8	1.7 ± 1.0
1094.8	0.3 ± 0.6	0.5 ± 1.0	-0.2 ± 1.3
1097.0	-0.2 ± 0.6	-0.2 ± 0.9	0.6 ± 1.2
1099.1	-0.2 ± 0.9	-1.5 ± 1.4	0.3 ± 1.7
1101.3	0.2 ± 0.4	0.0 ± 0.6	1.3 ± 0.7
1103.4	0.2 ± 0.5	0.9 ± 0.8	0.1 ± 1.0
1105.6	-0.2 ± 0.5	-0.4 ± 0.9	-0.5 ± 1.0
1107.7	0.4 ± 0.8	-0.1 ± 1.4	1.6 ± 1.7
1109.9	-0.5 ± 0.3	-0.4 ± 0.6	1.7 ± 0.7
1112.0	-0.8 ± 0.3	-0.5 ± 0.5	1.8 ± 0.7

TABLE III. (*Continued.*)

W (MeV)	$(a_1)_0$ (μb/sr)	$(a_1)_1$ (μb/sr)	$(a_1)_2$ (μb/sr)
1114.1	-1.2 ± 0.4	-1.0 ± 0.6	1.5 ± 0.8
1116.2	-0.7 ± 0.3	0.0 ± 0.5	1.8 ± 0.7
1118.3	-0.6 ± 0.3	0.1 ± 0.5	2.6 ± 0.7
1120.4	-1.5 ± 0.3	-1.0 ± 0.6	3.4 ± 0.7
1122.5	-1.3 ± 0.3	-0.6 ± 0.5	2.6 ± 0.6
1124.6	-1.5 ± 0.3	-0.5 ± 0.5	3.7 ± 0.7
1126.7	-1.8 ± 0.4	0.6 ± 0.7	2.6 ± 0.8
1128.8	-1.4 ± 0.3	0.3 ± 0.6	5.1 ± 0.8
1130.8	-1.8 ± 0.3	-1.3 ± 0.5	3.9 ± 0.7
1132.9	-1.8 ± 0.3	-0.5 ± 0.5	3.9 ± 0.7
1134.9	-2.4 ± 0.4	-0.2 ± 0.6	5.3 ± 0.8
1137.0	-1.9 ± 0.4	-0.5 ± 0.6	5.1 ± 0.8
1139.0	-2.6 ± 0.3	0.1 ± 0.5	5.5 ± 0.7
1141.0	-2.6 ± 0.5	0.7 ± 0.8	6.7 ± 1.1
1143.1	-2.4 ± 0.3	-0.5 ± 0.5	6.4 ± 0.8
1145.1	-2.6 ± 0.3	-0.4 ± 0.5	7.4 ± 0.8
1147.1	-3.0 ± 0.4	-0.3 ± 0.6	8.7 ± 1.0
1149.1	-2.9 ± 0.3	-0.5 ± 0.5	7.5 ± 0.8
1151.1	-3.8 ± 0.4	0.1 ± 0.5	9.1 ± 0.9
1153.1	-3.7 ± 0.4	-0.2 ± 0.5	9.1 ± 0.9
1155.0	-4.1 ± 0.4	-1.0 ± 0.5	9.9 ± 0.9
1157.0	-4.4 ± 0.4	-0.8 ± 0.5	10.4 ± 0.9
1159.0	-4.4 ± 0.4	-0.9 ± 0.5	10.8 ± 1.0
1160.9	-5.0 ± 0.5	-0.2 ± 0.5	11.2 ± 1.0
1162.8	-5.7 ± 0.5	-1.0 ± 0.5	11.5 ± 1.0

TABLE IV. Same as in Table III for 1164.8 MeV $\leqslant W \leqslant$ 1239.7 MeV.

W (MeV)	$(a_1)_0$ (μb/sr)	$(a_1)_1$ (μb/sr)	$(a_1)_2$ (μb/sr)
1164.8	-5.6 ± 0.5	-0.3 ± 0.5	12.7 ± 1.1
1166.7	-6.3 ± 0.5	-0.1 ± 0.5	13.9 ± 1.1
1168.6	-6.9 ± 0.6	-0.5 ± 0.5	14.3 ± 1.2
1170.5	-7.5 ± 0.6	0.1 ± 0.5	15.3 ± 1.2
1172.4	-7.8 ± 0.6	0.4 ± 0.4	15.8 ± 1.2
1174.3	-8.1 ± 0.6	0.6 ± 0.5	15.3 ± 1.2
1176.2	-8.7 ± 0.7	0.4 ± 0.5	17.5 ± 1.4
1178.0	-9.2 ± 0.7	0.5 ± 0.5	18.1 ± 1.4
1179.9	-9.7 ± 0.7	-0.1 ± 0.5	18.6 ± 1.4
1181.7	-10.2 ± 0.8	0.6 ± 0.5	19.6 ± 1.5
1183.6	-10.6 ± 0.8	0.2 ± 0.5	20.5 ± 1.6
1185.4	-11.1 ± 0.8	1.1 ± 0.4	21.1 ± 1.6
1187.2	-11.3 ± 0.9	0.9 ± 0.5	21.4 ± 1.6
1189.0	-12.2 ± 0.9	1.0 ± 0.5	22.8 ± 1.7
1190.8	-12.3 ± 0.9	1.0 ± 0.5	24.7 ± 1.8
1192.6	-13.0 ± 1.0	0.5 ± 0.5	24.4 ± 1.8
1194.4	-13.2 ± 1.0	0.9 ± 0.5	24.6 ± 1.8
1196.2	-13.9 ± 1.0	0.7 ± 0.5	25.5 ± 1.9
1197.9	-13.9 ± 1.0	0.3 ± 0.4	25.3 ± 1.9
1199.7	-13.9 ± 1.0	1.6 ± 0.5	26.6 ± 2.0
1201.4	-14.5 ± 1.1	1.2 ± 0.4	27.2 ± 2.0
1203.1	-14.8 ± 1.1	0.6 ± 0.5	26.7 ± 2.0
1204.8	-14.9 ± 1.1	1.5 ± 0.5	27.8 ± 2.1
1206.5	-15.0 ± 1.1	1.5 ± 0.5	26.6 ± 2.0
1208.2	-15.5 ± 1.1	1.8 ± 0.5	28.3 ± 2.1

TABLE IV. (*Continued.*)

W (MeV)	$(a_1)_0$ (μb/sr)	$(a_1)_1$ (μb/sr)	$(a_1)_2$ (μb/sr)
1209.9	-15.6 ± 1.2	1.6 ± 0.7	27.8 ± 2.1
1211.6	-15.9 ± 1.2	1.1 ± 0.5	28.2 ± 2.1
1213.2	-16.0 ± 1.2	1.2 ± 0.4	28.5 ± 2.1
1214.9	-16.1 ± 1.2	1.2 ± 0.4	28.9 ± 2.1
1216.5	-16.1 ± 1.2	0.5 ± 0.5	28.4 ± 2.1
1218.2	-16.0 ± 1.2	1.5 ± 0.4	28.7 ± 2.1
1219.8	-16.1 ± 1.2	2.3 ± 0.5	28.0 ± 2.1
1221.4	-16.1 ± 1.2	2.0 ± 0.6	28.2 ± 2.1
1223.0	-16.1 ± 1.2	1.9 ± 0.6	27.3 ± 2.1
1224.5	-15.6 ± 1.2	1.9 ± 0.5	27.5 ± 2.1
1226.1	-15.1 ± 1.1	1.4 ± 0.5	26.0 ± 1.9
1227.7	-15.4 ± 1.2	1.9 ± 0.6	26.2 ± 2.0
1229.2	-14.9 ± 1.1	1.9 ± 0.5	25.7 ± 1.9
1230.7	-15.0 ± 1.1	1.3 ± 0.4	26.3 ± 2.0
1232.3	-14.3 ± 1.1	1.9 ± 0.5	25.1 ± 1.9
1233.8	-14.4 ± 1.1	2.3 ± 0.5	25.6 ± 1.9
1235.3	-13.6 ± 1.0	1.4 ± 0.5	23.9 ± 1.8
1236.8	-13.4 ± 1.0	2.3 ± 0.5	24.1 ± 1.8
1238.2	-13.7 ± 1.0	1.1 ± 0.5	23.6 ± 1.8
1239.7	-13.2 ± 1.0	2.4 ± 0.5	22.8 ± 1.7

TABLE V. Same as in Table III for 1241.1 MeV $\leqslant W \leqslant$ 1276.3 MeV.

W (MeV)	$(a_1)_0$ (μb/sr)	$(a_1)_1$ (μb/sr)	$(a_1)_2$ (μb/sr)
1241.1	-12.7 ± 0.9	2.2 ± 0.5	23.2 ± 1.7
1242.6	-12.7 ± 1.0	1.5 ± 0.5	23.1 ± 1.8
1244.0	-12.2 ± 0.9	2.4 ± 0.6	21.8 ± 1.7
1245.4	-12.1 ± 0.9	1.8 ± 0.6	21.7 ± 1.7
1246.8	-12.2 ± 1.2	1.0 ± 0.7	21.8 ± 2.2
1248.2	-11.3 ± 0.9	2.0 ± 0.6	20.8 ± 1.6
1249.6	-10.9 ± 0.8	2.3 ± 0.6	19.8 ± 1.6
1251.0	-11.1 ± 0.9	2.2 ± 0.8	20.8 ± 1.7
1252.3	-10.5 ± 0.8	2.1 ± 0.5	18.4 ± 1.4
1253.7	-9.8 ± 0.8	1.4 ± 0.7	18.1 ± 1.5
1255.0	-10.2 ± 0.8	1.7 ± 0.7	18.2 ± 1.5
1256.3	-10.2 ± 0.9	1.4 ± 0.8	18.3 ± 1.6
1257.6	-9.8 ± 1.0	1.0 ± 1.1	18.4 ± 1.8
1258.9	-9.1 ± 0.8	2.0 ± 0.7	17.8 ± 1.5
1260.2	-8.9 ± 0.7	1.5 ± 0.7	17.9 ± 1.5
1261.5	-8.5 ± 0.7	2.3 ± 0.6	16.3 ± 1.4
1262.8	-8.7 ± 0.7	1.7 ± 0.7	15.0 ± 1.3
1264.0	-8.9 ± 0.7	1.7 ± 0.6	15.3 ± 1.3
1265.2	-8.4 ± 0.7	2.4 ± 0.7	16.0 ± 1.4
1266.5	-7.9 ± 0.7	3.3 ± 0.7	15.8 ± 1.4
1267.7	-7.9 ± 0.7	1.1 ± 0.7	13.4 ± 1.2
1268.9	-7.3 ± 0.8	1.0 ± 1.0	13.8 ± 1.6
1270.1	-7.3 ± 0.6	2.0 ± 0.6	13.6 ± 1.2
1271.3	-7.2 ± 0.6	2.4 ± 0.6	13.9 ± 1.2
1272.5	-7.6 ± 0.7	1.1 ± 0.7	14.0 ± 1.3
1273.7	-6.6 ± 0.5	1.1 ± 0.4	13.4 ± 1.1
1275.0	-6.3 ± 0.6	1.9 ± 0.7	12.1 ± 1.2
1276.3	-6.6 ± 0.6	1.6 ± 0.6	11.7 ± 1.1

[1] A. Bernstein and C. Papanicolas, AIP Conf. Proc. **904**, 1 (2007).
[2] C. Alexandrou, C. N. Papanicolas, and M. Vanderhaegen, Rev. Mod. Phys. **84**, 1231 (2012).
[3] B. Krusche and S. Schadmand, Prog. Part. Nucl. Phys. **51**, 399 (2003).
[4] R. Beck, H. P. Krahn, J. Ahrens, H. J. Arends, G. Audit, A. Braghieri *et al.*, Phys. Rev. Lett. **78**, 606 (1997).
[5] G. Blanpied, M. Blecher, A. Caracappa, R. Deininger, C. Djalali, G. Giordano *et al.*, Phys. Rev. C **64**, 025203 (2001).
[6] L. Tiator, D. Drechsel, S. Kamalov, and S. Yang, Eur. Phys. J. A **17**, 357 (2003).
[7] V. Pascalutsa and M. Vanderhaeghen, Phys. Rev. D **73**, 034003 (2006).
[8] T. A. Gail and T. R. Hemmert, Eur. Phys. J. A **28**, 91 (2006).
[9] T. Sato and T. S. H. Lee, Phys. Rev. C **63**, 055201 (2001).
[10] V. Pascalutsa and J. A. Tjon, Phys. Rev. C **70**, 035209 (2004).
[11] C. Fernández-Ramírez, E. Moya de Guerra, and J. M. Udias, Phys. Rev. C **73**, 042201(R) (2006).
[12] C. Alexandrou, G. Koutsou, J. W. Negele, Y. Proestos, and A. Tsapalis, Phys. Rev. D **83**, 014501 (2011).
[13] J. Ahrens (GDH and A2 Collaborations), Eur. Phys. J. A **21**, 323 (2004).
[14] R. Beck, H. P. Krahn, J. Ahrens, J. R. M. Annand, H. J. Arends, G. Audit *et al.*, Phys. Rev. C **61**, 035204 (2000).
[15] R. Beck, R. Leukel, and R. Schmidt, Acta Phys. Pol. **B33**, 813 (2002).
[16] C. Galler *et al.*, Phys. Lett. B **503**, 245 (2001).
[17] R. Workman *et al.* (Particle Data Group), Prog. Theor. Exp. Phys. **2022**, 083C01 (2022).
[18] L. Markou, E. Stiliaris, and C. Papanicolas, Eur. Phys. J. A **54**, 115 (2018).
[19] E. Stiliaris and C. N. Papanicolas, AIP Conf. Proc. **904**, 257 (2007).
[20] C. Alexandrou, T. Leontiou, C. N. Papanicolas, and E. Stiliaris, Phys. Rev. D **91**, 014506 (2015).
[21] H. Kaiser *et al.*, Nucl. Instrum. Methods Phys. Res., Sect. A **593**, 159 (2008).
[22] E. Mornacchi, Ph.D. thesis, University of Mainz, 2021, http://doi.org/10.25358/openscience-6051.
[23] L. Witthauer *et al.* (A2 Collaboration at MAMI), Eur. Phys. J. A **49**, 154 (2013).
[24] D. Werthmüller *et al.* (A2 Collaboration at MAMI), Phys. Rev. C **90**, 015205 (2014).
[25] M. Dieterle *et al.* (A2 Collaboration at MAMI), Phys. Lett. B **770**, 523 (2017).
[26] L. Witthauer *et al.* (A2 Collaboration at MAMI), Phys. Rev. C **95**, 055201 (2017).
[27] M. Dieterle *et al.* (A2 Collaboration at MAMI), Phys. Rev. C **97**, 065205 (2018).
[28] F. Cividini *et al.* (A2 Collaboration at MAMI), Eur. Phys. J. A **58**, 113 (2022).
[29] V. Tioukine, K. Aulenbacher, and N. Riehn, Rev. Sci. Instrum. **82**, 033303 (2011).
[30] J. C. McGeorge *et al.*, Eur. Phys. J. A **37**, 129 (2008).
[31] H. Olsen and L. Maximon, Phys. Rev. **114**, 887 (1959).
[32] C. Rohlof and H. Dutz, in *Proceedings of the 2nd International Symposium on the Gerasimov-Drell-Hearn Sum Rule and the Spin Structure of the Nucleon (GDH 2002)* (World Scientific, Singapore, 2002), pp. 201–205.
[33] S. T. Goertz *et al.*, Nucl. Instrum. Methods Phys. Res., Sect. A **526**, 43 (2004).
[34] Ch. Bradtke *et al.*, Nucl. Instrum. Methods Phys. Res., Sect. A **436**, 430 (1999).
[35] D. Paudyal, Ph.D. thesis, University of Regina, 2017, http://wwwa2.kph.uni-mainz.de/images/publications/phd/Paudyal-PhD-thesis.pdf.
[36] D. Paudyal *et al.* (A2 Collaboration), Phys. Rev. C **102**, 035205 (2020).
[37] A. Starostin, B. M. K. Nefkens, E. Berger, M. Clajus, A. Marusic, S. McDonald, N. Phaisangittisakul *et al.*, Phys. Rev. C **64**, 055205 (2001).
[38] R. Novotny *et al.*, IEEE Trans. Nucl. Sci. **38**, 379 (1991).
[39] A. R. Gabler *et al.*, Nucl. Instrum. Methods Phys. Res., Sect. A **346**, 168 (1994).
[40] S. Agostinelli *et al.*, Nucl. Instrum. Methods Phys. Res., Sect. A **506**, 250 (2003).
[41] A. V. Anisovich *et al.*, Eur. Phys. J. A **52**, 284 (2016).
[42] W. J. Briscoe, A. Schmidt, I. Strakovsky, R. L. Workman, and A. Švarc (SAID Group), Phys. Rev. C **108**, 065205 (2023).
[43] S. S. Kamalov and S. N. Yang, Phys. Rev. Lett. **83**, 4494 (1999).
[44] S. S. Kamalov, S. N. Yang, D. Drechsel, O. Hanstein, and L. Tiator, Phys. Rev. C **64**, 032201(R) (2001).
[45] S. S. Kamalov, D. Drechsel, L. Tiator, and S. N. Yang, in *Proceedings of the 2nd International Workshop on the Physics of Excited Nucleons* (World Scientific, Singapore, 2001), pp. 197–202.
[46] L. Tiator, S. S. Kamalov, S. Ceci, G. Y. Chen, D. Drechsel, A. Svarc, and S. N. Yang, Phys. Rev. C **82**, 055203 (2010).
[47] S. Hoblit, A. M. Sandorfi, K. Ardashev, C. Bade, O. Bartalini, M. Blecher *et al.* (LETS-Spin Collaboration), Phys. Rev. Lett. **102**, 172002 (2009).
[48] P. Adlarson *et al.* (A2 Collaboration at MAMI), Phys. Rev. C **92**, 024617 (2015).
[49] F. Afzal *et al.* (A2 Collaboration at MAMI) [Phys. Rev. Lett. (to be published)].
[50] Y. Wunderlich, F. Afzal, A. Thiel, and R. Beck, Eur. Phys. J. A **53**, 86 (2017).
[51] G. D'Agostini, Nucl. Instrum. Methods Phys. Res., Sect. A **346**, 306 (1994).
[52] P. Pedroni and S. Sconfietti, J. Phys. G: Nucl. Part. Phys. **47**, 054001 (2020).
[53] B. Pasquini, P. Pedroni, and S. Sconfietti, Phys. Rev. C **98**, 015204 (2018).
[54] B. Pasquini, P. Pedroni, and S. Sconfietti, J. Phys. G: Nucl. Part. Phys. **46**, 104001 (2019).
[55] E. Mornacchi, S. Rodini, B. Pasquini, and P. Pedroni, Phys. Rev. Lett. **129**, 102501 (2022).
[56] Y. Wunderlich, Ph.D. thesis, University of Bonn, 2019, https://hdl.handle.net/20.500.11811/7868.
[57] R. A. Arndt, W. J. Briscoe, I. I. Strakovsky, and R. L. Workman, Phys. Rev. C **66**, 055213 (2002).
[58] G. Chew, F. Goldberger, F. Low, and Y. Nambu, Phys. Rev. **106**, 1345 (1957).
[59] R. A. Arndt *et al.*, in *Proceedings of the 2nd International Workshop on the Physics of Excited Nucleons* (World Scientific, Singapore, 2001), pp. 467–492.